Fabrication and characterization of graphene-based carbon hollow spheres for encapsulation of organic corrosion inhibitors

Haddadi, S. A.; Ramazani, S. A.A.; Mahdavian, M.; Taheri, P.; Mol, J. M.C.

DOI
10.1016/j.cej.2018.06.063

Publication date
2018

Document Version
Final published version

Published in
Chemical Engineering Journal

Chemical Engineering Journal 352 (2018) 909–922

Contents lists available at ScienceDirect

Chemical Engineering Journal

journal homepage: www.elsevier.com/locate/cej

Fabrication and characterization of graphene-based carbon hollow spheres for encapsulation of organic corrosion inhibitors

S.A. Haddadi[a], S.A.A. Ramazani[a,*], M. Mahdavian[b], P. Taheri[c], J.M.C. Mol[c]

[a] Chemical and Petroleum Engineering Department, Sharif University of Technology, PO Box 11155-9465, Tehran, Iran
[b] Surface Coating and Corrosion Department, Institute for Color Science and Technology, PO Box 54-16765, Tehran, Iran
[c] Department of Materials Science and Engineering, Delft University of Technology, 2628CD Delft, The Netherlands

HIGHLIGHTS

- Graphene-based CHSs were synthesized for MBI corrosion inhibitor encapsulation.
- The carbon structure of the shells was characterized by Raman spectroscopy and XRD.
- pH-dependent release of MBI from the carbon capsules was evaluated using UV–vis.
- MBI release from carbon capsules increased with the pH of the NaCl solution.
- MBI released from CHSs forms a protective film on mild steel retarding corrosion.

GRAPHICAL ABSTRACT

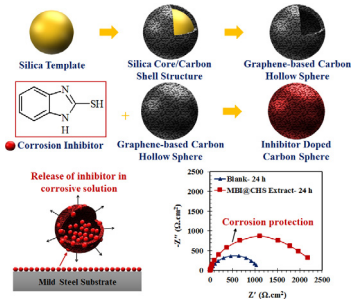

ARTICLE INFO

Keywords:
Graphene-structure
Carbon hollow sphere
Hard template
Corrosion inhibitor

ABSTRACT

In this work, we synthesized carbon hollow spheres (CHSs) using the silica templating method, encapsulated 2-mercaptobenzimidazole (MBI) inhibitor in the CHSs and evaluated their corrosion inhibition performance upon exposure of mild steel to a saline solution containing the released inhibitor. The effects of silica template surface modification on the CHS structure was evaluated, while the structure and morphology of the synthesized CHS was analyzed using field emission scanning electron microscope (FE-SEM), transmission electron microscope (TEM), Raman spectroscopy and X-ray diffraction (XRD) spectroscopy. Furthermore, thermogravimetric analysis (TGA), energy-dispersive X-ray spectroscopy mapping (EDS-mapping) and UV–vis were employed to evaluate the MBI release from carbon capsules at different pH values. Corrosion protection performance of the doped CHS was evaluated using potentiodynamic polarization and electrochemical impedance spectroscopy (EIS) techniques. The results showed tunability of the shell structure between an amorphous carbon and graphene structure using surface modification of the silica templates. Moreover, the MBI release from the CHSs showed to be pH-dependent allowing smart protection of mild steel when exposed to corrosive conditions.

1. Introduction

Corrosion inhibitors are generally used to protect metallic surfaces in corrosive media. Direct incorporation of corrosion inhibitors in organic protective coatings may lead to reduction of their barrier and mechanical properties due to possible interference of the inhibitor with

* Corresponding author.
E-mail address: ramazani@sharif.edu (S.A.A. Ramazani).

https://doi.org/10.1016/j.cej.2018.06.063
Received 9 March 2018; Received in revised form 14 May 2018; Accepted 10 June 2018
Available online 15 June 2018
1385-8947/

functional groups and curing reactions of the coatings [1,2]. One of the common strategies is the encapsulation of corrosion inhibitors in micro/nano containers to control the release of inhibitors and increase the durability and protection efficiency of the coatings [1]. Self-healing polymer coatings containing containers doped with active agents are used increasingly for extending the substrate life-time upon the occurrence of coating damage [3–7]. Recently, micro/nano containers such as zinc phosphate, double layered hydroxyl (LDH) pigments [8,9], halloysite [10], montmorillonite [11], metal-organic structures, mineral and organic containers [4,12] doped with corrosion inhibiting agents are used to fabricate self-healing and smart coatings. Despite the capability of the capsules to contain the active agents, they suffer from substantial drawbacks such as unchangeable specific volume, poor mechanical properties and thermal and chemical instability [13–15]. Tedim et al. [16] evaluated the active corrosion protection performance and efficiency of LDH containers doped with vanadate, phosphate and 2-mercaptobenzothiazole in sodium chloride solution. The release of benzotriazole from layer-by-layer nanocontainers based on zinc molybdate was studied by Karekar et al. [17]. Jadhav et al. investigated synthesis, corrosion protective properties and controlled release of imidazole from layer by layer assembled zinc phosphate nanoparticles [18–20]. The obtained results showed that the release of the organic inhibitors from the micro/nano containers could protect the metallic substrates and enhance the corrosion protection performance of the coatings.

Corrosion inhibitors could be categorized to the organic inhibitors and active inorganic pigments [21,22]. Among the organic components, mercaptocarboxilic acids, azoles, thioglycolate esters, organic phenols, sulfides, phosphates and amines could form protective thin films on the surface of metals [23]. The inhibition performance of the organic coatings depends on the type, distribution and concentration of the inhibitors in the system. Incorporation of the organic inhibitors in protective overlayers such as organic coatings leads to the enhancement of barrier properties of the coatings and formation of passive films at the metal/coating interface [16,23].

Carbon in different configuration, e.g. fullerenes, graphite, graphene and carbon nanostructures have been used for different advanced applications such as batteries, energy and hydrogen storage systems, catalyst, sensors, membranes, etc. [24–29]. Carbon hollow spheres (CHSs) represent a new class of carbon nanostructures attracting substantial attention due to its exceptional characteristics such as excellent mechanical strength and thermal conductivity as well as tunable shell structure, porosity, thickness and size [29,30], making them excellent candidates for high-tech applications such as supercapacitors [31], lithium-sulfur batteries [32,33], fuel cells, solar cells and nanoelectrodes [8,34–37]. While most of prior studies deal with the CHS synthesis and fabrication of mesoporous carbon spheres for encapsulation of chemicals into the CHSs for drug delivery purposes [26,38], there is no record on the encapsulation of corrosion inhibitors in CHSs for smart corrosion protective coatings.

CHSs reported in literature were synthesized by different methods such as chemical vapor deposition [39], self-assembly [27], carbonization and templating [26,40]. Templating, used for the preparation of the core material, can be classified in soft templating and hard templating approaches [26,41]. For the hard templating routes, rigid particles such as polystyrene (PS) [28] and silica [41,42] are employed as the hard core is sacrificed after formation of the carbon-based shell. In order to prepare the shell, the carbon precursor, e.g. sucrose, glucose, furfuryl alcohol, pitch and phenol, is turned to a carbon structure after carbonization at high temperatures [26,30]. Carbonization parameters such as temperature, time, atmosphere and surface chemistry of the hard templates determine the carbon structure type [28,29,43].

In this work, we have synthesized CHSs using the silica templating method and encapsulated them with MBI as a typical corrosion inhibitor for mild steel. Moreover, a surface treatment was applied on the silica templates to alter the surface structure and consequently the surface charge. The pH triggered release of MBI from the doped CHS was studied using UV–vis and the corrosion inhibition of the system was evaluated by means of electrochemical measurements.

2. Experimental

2.1. Chemicals

Tetraethyl orthosilicate (TEOS, ≥98%) as a silicon dioxide precursor, aqueous ammonia (28 wt%) as a catalyst of sol-gel reactions, (3-aminopropyl) triethoxysilane (APTES, ≥99%) as a surface modifier and MBI (≥98%) as a corrosion inhibitor were supplied by Sigma-Aldrich. Sucrose (≥98%) was purchased from Chem-Lab and used as a carbon precursor for fabrication of the carbon shells. Absolute ethanol (99.6%) was used as a supporting electrolyte to synthesize the silica templates purchased from Arak Distillation Co. Sodium hydroxide (NaOH, ≥99%) and hydrochloric acid (HCl, 37 wt%) were used for pH adjustment, while sodium chloride (NaCl, ≥99%) was used for preparation of the saline corrosive medium and hydrofluoric acid (HF, 40 wt%) was used for the silica core removal, all supplied by Mojalali Co. Double distilled and DI water were used for washing and preparation of the solutions, respectively. Mild steel panels (99.01 wt% Fe, 0.34 wt% Si, 0.32 wt% Mn, 0.19 wt% C, 0.05 wt% S, 0.05 wt% P and 0.04 wt% Al) were purchased from Foolad Mobarake Co. Argon gas with purity of 99.99% was provided by Arkan Gas Co. Industrial grades of columns of P_2O_5, KOH and activated 13X/4A type molecular sieves (Arak Petrochemical Co.) were used for dehydration and purification. Other chemicals were used as received.

2.2. Synthesis of CHS

Synthesis of silica templates with an average particle size of 260 nm was performed in an alkali ethanol-water solution according to the Stober's method [44]. Ethanol (13 ml), DI water (0.5 ml) and aqueous ammonia (1.5 ml) were added into an Erlenmeyer flask of 25 ml. Then, a uniform mixture of ethanol (5 ml) and TEOS (0.5 ml) was prepared and added dropwise to the solution made earlier under continuous stirring of 300 rpm at 30 °C. After 3 h, the synthesized silica template was extracted by centrifugation (7000 rpm, 10 min) and washed with ethanol and double distilled water for several times.

In order to chemically modify the surface chemistry of synthesized silica templates with APTES, the synthesized silica nanoparticles (1 g) were dissolved in absolute ethanol (80 ml) in a glass container equipped with a reflux column. Consequently, 2 ml of APTES was added directly to the solution under continuous stirring (110 rpm) at 70 °C. In order to graft APTES properly to the surface of CHSs, the solution was continuously stirred for 36 h. Then, the precipitation was collected using centrifugation (7000 rpm, 10 min), washed with absolute ethanol for three times and dried in a vacuum oven at 110 °C for 6 h.

Polysaccharide shells were fabricated on the modified and unmodified silica templates by means of hydrothermal treatment in an aqueous sucrose. The silica templates (1 g) were dispersed uniformly into a 0.5 mol l^{-1} aqueous sucrose solution. Then, the suspension was transferred into a 50 ml Teflon-sealed autoclave at 190 °C for 3 h. Next, the precipitation was collected using centrifugation (5000 rpm, 5 min) and washed with ethanol and double distilled water for three times and dried in a vacuum oven at 50 °C for 12 h. Carbonization of the polysaccharide coated silica templates was carried out at 900 °C in a tubular furnace (AZAR FURNACE, TF5/40-1250, Iran) under argon atmosphere for 3 h to obtain the silica core/carbon shell structure. Finally, the silica templates were removed by 10% aqueous hydrofluoric acid solution for 2 h to form the CHSs. After the silica core removal, the procedure conducted for the surface modification of silica templates was repeated for the surface modification of CHSs.

2.3. Encapsulation of corrosion inhibitor

In order to encapsulate MBI into CHSs, a 0.2 g CHSs was added into a 40 ml of MBI solution in absolute ethanol with concentration of 35 mg ml^{-1} (35,000 ppm) under stirring at 110 rpm for 12 h. Afterwards, the suspension was transferred into a round-bottom flask evacuated by a vacuum pump for 30 min under continuous stirring to ensure a complete release of the trapped air and to maximize loading of the inhibitor in the CHSs. Finally, the MBI doped CHSs were collected using centrifugation (7000 rpm, 10 min), washed with mixture of ethanol and water for three times and dried at 50 °C for 12 h. The MBI doped CHS is called MBI@CHS in this work.

2.4. Preparation of samples and test solutions

To prepare the extract solution, a 1 g of the MBI@CHS was suspended uniformly into a 1 L of 3.5 wt% NaCl solution under stirring conditions (110 rpm) for 24 h. Then, the suspension was centrifuged (7000 rpm, 10 min) to obtain the extract solution. The 3.5 wt% NaCl solution without MBI@CHS was used as the blank solution for comparison.

Mild steel panels (8 cm × 3 cm × 0.2 cm) were polished with emery papers No. 200, 400, 800, 1200 and 1500, respectively followed by degreasing in acetone. Exposed areas of 1 cm^2 were used for the electrochemical measurements and the rest areas of the samples were sealed with a hot mixture of beeswax and colophony (in 3:1 wt% ratio). The polarization and EIS measurements were repeated three times to ensure reproducibility of the results.

2.5. Release of corrosion inhibitor at different pHs

In order to investigate the release of MBI from MBI@CHS at different pHs, the doped capsules were suspended in the HCl solution with pH = 3, DI water with pH = 7 and NaOH solution with pH = 11. The concentration of released MBI during certain period of time was measured using UV–vis spectroscopy. Calibration curves were recorded for each pH containing certain concentration of MBI.

2.6. Characterization techniques

2.6.1. Characterization of CHSs

Morphology of the synthesized silica templates and CHSs was evaluated using FE-SEM (Mira 3-XMU, TESCAN, Czech Republic) and TEM (EM 900, ZEISS, Germany). Droplets of diluted suspensions of silica and CHS were placed on clean aluminum foils and let them to dry. To avoid surface charging, the samples were double-coated with gold and elemental maps of carbon (C), sulfur (S), nitrogen (N) and oxygen (O) were collected using EDS (Oxford Instruments, United Kingdom). Surface morphologies and the elemental mapping of C, S and N for the mild steel samples after 24 h exposure to the test solutions were evaluated using FE-SEM (Jeol, JSM-6500F, Japan).

Nitrogen (N_2) physisorption measurements were conducted using BELSORP-mini II instrument at −200 °C after a pretreatment at 250 °C under the vacuum for 8 h. The specific volume and surface area, pore volume and pore size distribution of the silica core/carbon shell and CHS structures were determined using Brunauer-Emmett-Teller (BET) and Barrett-Joyner-Halenda (BJH) methods. Raman spectra of CHSs synthesized using unmodified and modified silica templates were determined by means of Handheld Raman analyzer (Firstguard, Rigaku, Japan) at Raman shift range of 1200–2700 cm^{-1}. XRD spectra of the silica templates, silica core/carbon shell and CHS structures were obtained using a X-pert Philips diffractometer (PW 3040/60, The Netherlands) with an Cu-$K_{\alpha 1}$ radiation (λ = 1.54 Å), copper anode and graphite monochromator. The XRD patterns were obtained at 2θ range from 10° to 75° with the scanning rate of 2.5° min^{-1}, and the accelerating voltage and current of 40 kV and 20 mA, respectively. To assess the chemical composition and grafting of APTES onto the surface of the silica templates and CHSs before and after surface modification with amino groups, a Fourier transform infrared spectrometer (FTIR, Bruker, Tensor 27, Germany) was employed to measure the molecular vibrations within the wavenumber range of 400–4000 cm^{-1}. The samples in the form of KBr pellets were used for FTIR spectroscopy. Also, a confocal FTIR spectrometer (Thermo SCIENTIFIC, NICOLET 6700, USA) was employed in order to evaluate the chemical composition of the rusts and corrosion products formed on the mild steel surface immersed in the test solutions.

2.6.2. Characterization of the MBI loaded CHSs

TGA analysis was used to estimate the extent of MBI encapsulated into CHSs using a LINSEIS analyzer (L-801I, Germany) from ambient temperature to 700 °C at a heating rate of 10 °C min^{-1} under an argon atmosphere. Concentration of the released MBI into the solutions was determined using a UV–vis spectrometer (RAYLEIGH, UV-2601, China). Zeta potentials (surface charge) of the CHSs dispersed into the aqueous solutions with different pHs were measured using a Malvern zeta potential analyzer (3000HS, United Kingdom). The pHs of the solutions were adjusted by gradual addition of the diluted HCl (0.1 M) or NaOH (0.1 M) solutions.

2.6.3. Electrochemical measurements

Open circuit potential (OCP) values were monitored during 24 h of exposure of steel samples to the test solutions. Polarization and EIS measurements were conducted on mild steel samples (1 cm^2) after 1, 4 and 24 h immersion in the test solutions using a three-electrode cell including saturated calomel electrode (SCE, 3 M KCl), platinum and the mild steel samples as reference, counter and working electrodes, respectively. The polarization tests were carried out using a CorrTest (CS350, China) from −200 mV to +200 mV at a scan rate of 0.5 mV s^{-1}. The EIS measurements were implemented in the frequency range of 10 kHz–10 mHz at open circuit potential (OCP) with 10 mV perturbation. The obtained spectra were analyzed using CorrTest software.

3. Results and discussion

3.1. Characterization of nanostructured CHS capsules

3.1.1. FE-SEM

The morphology of the synthesized silica templates before and after hydrothermal and carbonization treatment is illustrated in Fig. 1. It can be seen that the synthesized silica templates are spherical in all steps with an average diameter of ~240 nm. Moreover, the synthesized silica templates are monodisperse with a narrow size distribution due to the catalysis effect of ammonia in the Stober method [44]. Accordingly, the alcohol and catalyst type as well as the water, alcohol and TEOS proportions into the synthesis media affect the monodispersity, morphology and size of the synthesized silica particles. As shown in Fig. 1b, after the hydrothermal treatment of the surface modified silica templates, the small polysaccharide particles disappear. This is due to the fact that polysaccharide tends to polymerize onto the surface of the modified spherical silica templates and form a silica core/polysaccharide shell structure with a uniform spherical morphology [41,45]. Surface modification of the silica nanoparticles with aminosilane makes the silica surfaces positively charged. Thus, saccharide molecules with negative surface charge can adsorb and condense properly on silica surfaces. The efficiency of the hydrothermal process is decreased in the presence of the unmodified silica templates. In fact, synthesized silica particles in presence of ammonia catalyst have a negative surface charge because of the surface hydroxyl groups. Hydrothermal process of the saccharide solution in presence of the negatively charged silica particles leads to formation of the spherical polysaccharide particles while the saccharide chains have no tendency to

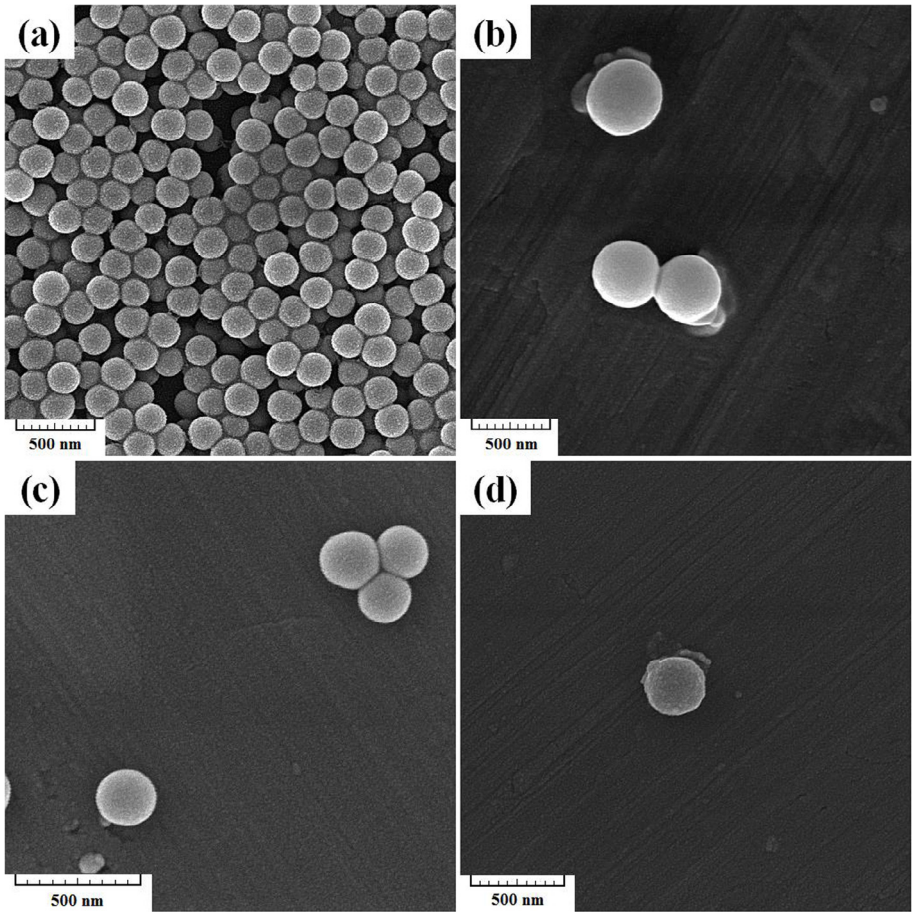

Fig. 1. FE-SEM images of the synthesized silica templates (a), silica core/polysaccharide shell structure (b), silica core/carbon shell structure (c) and CHS (d).

cover the surface of the silica nanoparticles [41]. This phenomenon leads to formation of the physically adsorbed polysaccharide shells and carbon with more sp^3 structures after carbonization on the surface of silica templates [41,45].

3.1.2. TEM

TEM was employed to evaluate the structural morphology of the synthesized silica core/carbon shell before and after the silica core removal. TEM images of the synthesized silica core/carbon shell and CHS are shown in Fig. 2. Fig. 2a shows a spherical morphology of the synthesized silica core/carbon shell structures which is in agreement with FE-SEM results. The observed dark regions in the center of the particles are attributed to the silica core. As indicated by formation of transparent regions in centers of the particles shown in Fig. 2b, the silica cores are removed after the treatment in the aqueous HF solution. A comparison of Fig. 2a and b shows that the silica core removal has no significant influence on the original spherical morphology of the particles. Earlier studies reported that the thickness of the polysaccharide

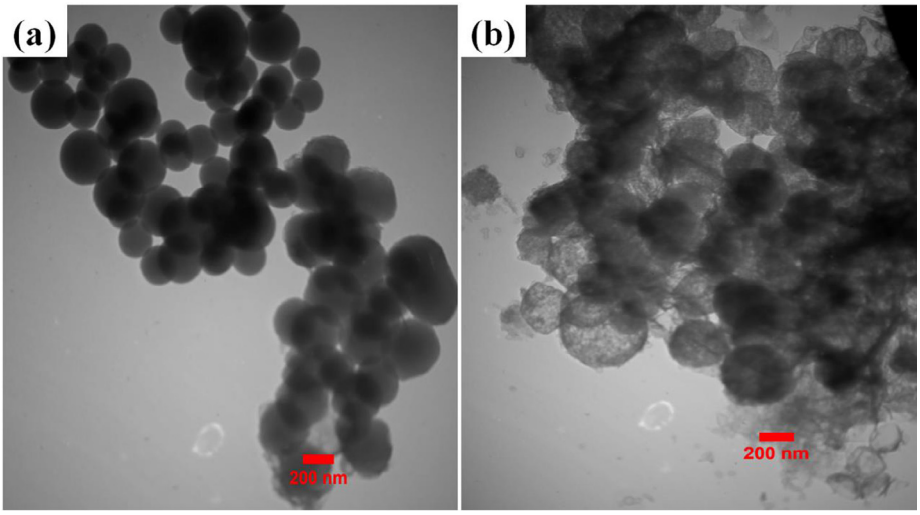

Fig. 2. TEM images of the silica core/carbon shell structure before (a) and after (b) the silica core removal.

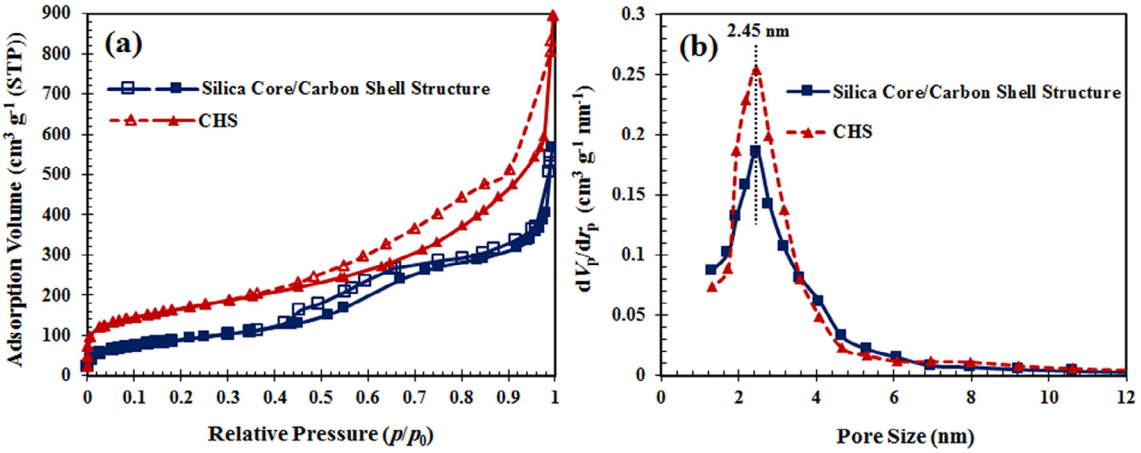

Fig. 3. N_2 adsorption-desorption isotherms (a) and pore size distribution (b) of the silica core/carbon shell structure and CHS.

shell onto the surface of the silica templates may change from ≤10 nm to ≥30 nm, depending on the hydrothermal conditions, such as the aqueous sucrose solution concentration, duration and temperature of hydrothermal process and surface chemistry of the silica templates [28,29]. Moreover, during the polysaccharide shell carbonization and the consequent release of the volatile components, the polysaccharide shell shrinks forming nano-sized pores on the shell [41]. Therefore, it can be inferred that the HF solution penetrates via these pores to remove the silica templates from the inside.

3.1.3. N_2 adsorption-desorption isotherms

The N_2 adsorption-desorption technique was used to determine the specific surface area and volume, total pore diameter and mean pore diameter values of the silica core/carbon shell before and after silica core removal using BET and BJH methods.

The N_2 adsorption-desorption isotherms and pore size distribution of the silica core/carbon shell nanostructures before and after the core removal are presented in Fig. 3a. A mesoporous structure of CHSs can be proven by a type H3 hysteresis located in a relative pressure of 0.41–0.95 for the IV-shaped isotherm of CHS according to the IUPAC classification [30,46]. The microporous structure of silica core/carbon shell is related to the nanoporosity of the carbon shell itself while the porosity of the CHS samples originates from both the interior region and carbon shell nanoporosity according to Fig. 3b.

The specific volume and surface area, total pore diameter and mean pore diameter values are calculated using BET and BJH methods as summarized in Table 1. As expected, the BET surface area and volume and BJH average pore diameter for CHSs are found to be higher than that of the silica core/carbon shell structure due to the silica template removal. This can be due to the fact that removal of the silica core increases the specific surface area and vacant volume of CHSs to ~77% in comparison with the silica core/carbon shell while the mean pore diameter is approximately the same for both samples. In addition, the increment of a_s and V_m of CHSs after acid treatment proves the successful removal of the silica templates. Consequently, with removal of the silica core, more volume and surface area are obtained to dope the corrosion inhibitor into the CHSs. Li et al. [47] and Fang et al. [48] showed that the removal of templates from core/shell structures resulted in an increment of the specific surface area and volume. As shown in Fig. 3b, the pore size distribution obtained by the BJH method for both samples illustrates one peak at ~2.45 nm while the mean pore size for the synthesized CHSs was ~4 nm as reported by Ikeda et al. [41]. It can be inferred from this result that the mean pore size of the carbon shell can be altered by changing the synthesis parameters.

3.1.4. Raman spectroscopy

Raman spectroscopy was employed to evaluate the effects of silica template surface modification on the structure of the carbon shell. Raman spectra of the synthesized CHSs using the unmodified and modified silica templates and the high resolution Raman spectra at D, G and 2D bands are shown in Fig. 4a and b, respectively. The G band is the in-plane vibrational state related to the sp^2 hybridized carbon atoms comprising the graphene sheets. For graphene, the G band is a sharp peak and its position is highly sensitive to the number of layers [49,50]. The D band which is also introduced as the disorder band originates from a ring breathing state of sp^2 carbon rings [49]. Intensity of the D band is related to the defect density. The 2D band or the second order of D band, originates from a two phonon lattice vibrational process. The 2D band does not present the structural defects. The number of layer can be determined by not only the peak position, but also the shape of the 2D band [49,51].

According to Fig. 4a, the D, G and 2D bands of the synthesized CHSs appear at ~1277, ~1598 and ~2614 cm^{-1}, respectively. As shown in Fig. 4a, the intensity proportions of the G band to the D band (I_G/I_D) of the CHSs formed on the surface of the unmodified and silanized silica templates are ~0.75 and ~1.51, respectively. The I_G/I_D value is higher than 1 for the CHSs synthesized via the modified silica templates indicating that the formed carbon shells are largely graphitized possessing lower structural defects with sp^2 carbon structures. However, in the presence of unmodified silica templates the I_G/I_D value is smaller than 1 indicating the formation of sp^3 carbon shells. Formation of sp^2 or sp^3 carbon structures influences the physicomechanical properties, overall efficiency and permeability of the doped active agents [26]. For successful encapsulation of the active agents, carbon shells with high mechanical strength are required. It is reported that the doped carbon shells with sp^3 carbon structure exhibit relatively weak mechanical properties resulting in damage of the capsule during the doping process, whereas sp^2 carbon structures present better mechanical properties.

Table 1
The N_2 adsorption-desorption isotherm values obtained by BET and BJH methods.

Sample	Specific surface area (a_s)/m^2 g^{-1}	Specific volume (V_m)/cm^3 g^{-1}	Total pore volume/cm^3 g^{-1}	Mean pore diameter/nm
Silica core/carbon shell structure	326	75	0.8	3.1
CHS	579	133	1.3	3.4

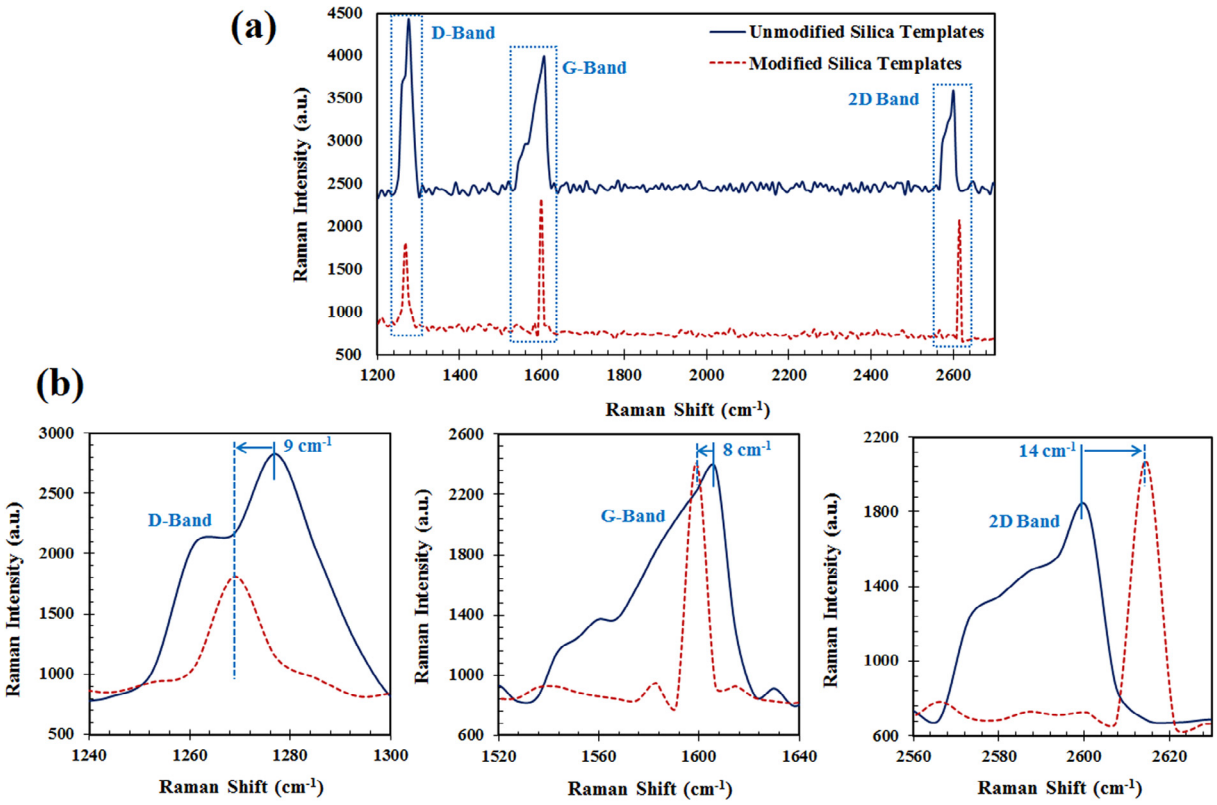

Fig. 4. Raman spectra of the synthesized CHSs using unmodified and modified silica templates (a) and the high resolution Raman spectra at D, G and 2D bands (b).

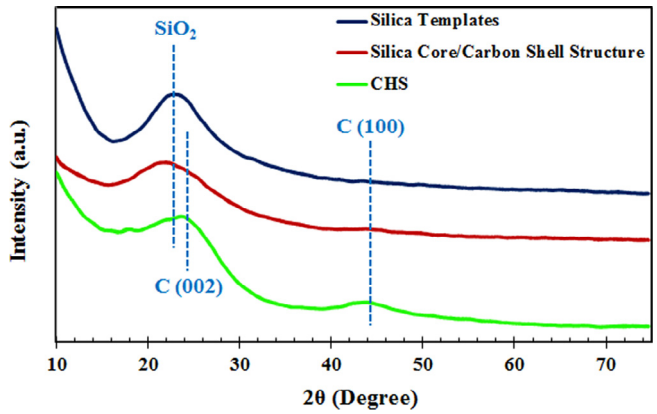

Fig. 5. XRD patterns of the silica templates, silica core/carbon shell structure and CHS.

Table 2
XRD data of CHS sample calculated using the Scherrer method and Bragg law.

Peak position (°)	$\beta_{Struct.}$ (°)	L (Å)	$d_{spacing}$ (Å)	Number of graphene layers
24.2	5.3	15	3.7	5

Therefore, it can be inferred that fabrication of CHSs synthesized via the modified silica templates is beneficial to obtain robust capsules.

In graphene-like structures, the 2D band is a sharp strong symmetric peak. With a decrement of the graphene layers, the shape of the peak changes to a wide peak formed due to overlaps of different layer interactions [49]. According to the literature [49,50], for graphene compared to graphite with the low structural defects, D and G bands shift to a lower energy while the 2D band shifts to a higher energy, sharpening the peak to an asymmetric shape. As shown in Fig. 4b, the D, G and 2D bands of the CHSs are overlapping which can be attributed to the presence of an asymmetric graphite structure with extensive structural defects and impurities. However, the D and 2D and G bands of the CHSs synthesized with the silanized silica templates are symmetric and sharp showing ~9, ~8 and ~14 cm^{-1} Raman shifts, respectively. These shifts indicate that the surface modification of the silica templates prepares an appropriate surface for the polysaccharide molecules to adsorb and then polymerize uniformly on the surface of the silica templates to form the symmetric graphene-like structures after carbonization.

In fact, after surface modification of the silica templates by APTES, the polysaccharide molecules fully cover silica template surfaces and form uniform layered shells due to the enhancement of the electrostatic interactions between saccharide molecules and surfaces of the modified silica templates with amino groups. Also, formation of the hydrogen bonds between the hydroxyl groups of saccharide molecules and amino groups of the surface modified silica templates lead to the formation of the uniform polysaccharide shells on the silica template surfaces. The 2D band change from the wide overlapped band to a symmetric sharp band for the synthesized CHSs with the silanized silica template indicates transformation of the carbon shells from a graphene-like structure with many defects to graphene having < 10 layers [52].

3.1.5. XRD spectroscopy

The Raman results showed that surface modification of silica templates leads to formation of a symmetric graphene-structure. XRD is employed to investigate the structure of the silica templates in more detail. XRD patterns of the silica templates and silica templates/core shell before and after silica removal are shown in Fig. 5. The broad peak at 2θ = 22.4° can be attributed to the amorphous structure of SiO_2 as hard templates [53]. The intense peaks at 2θ = 24.2° and the small peaks at 2θ = 42.2° are indexed to the C (0 0 2) and C (1 0 0) reflection of the hexagonal graphene structure, respectively [29,54]. It should be noted that for the silica core/carbon shell structure, the relatively low

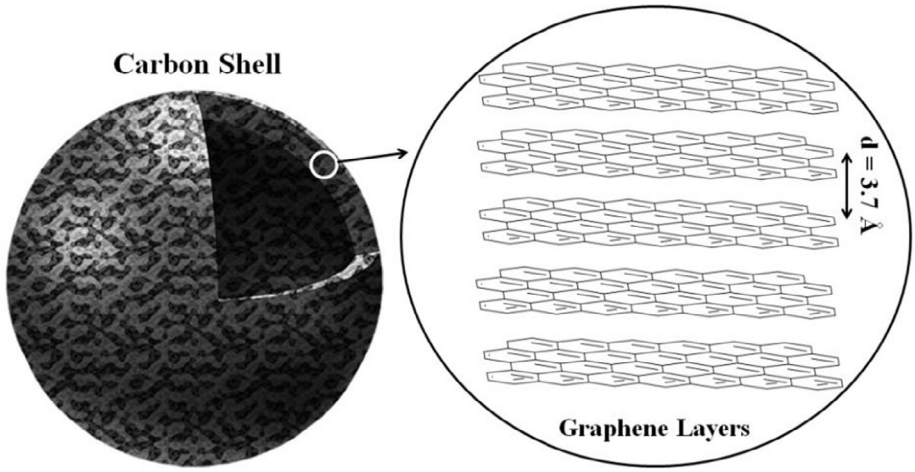

Fig. 6. Graphene structure of the CHS shell.

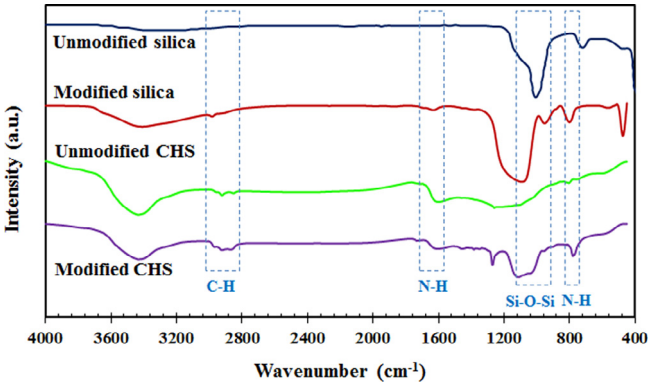

Fig. 7. FTIR spectra of the silica templates and CHS before and after surface modification with amino groups.

thickness of carbon shell leads to the lower intensity of the C (0 0 2) and C (1 0 0) reflection peaks compared to the silica reflection peak. The main portion of the ejected electrons from the surface originates from the silica core rather than from the carbon shell. Additionally, the silica core is structurally amorphous which in-turn expands the peak width resulting in the wider appearance of the peaks presented. Furthermore, the weight and volume ratios of the silica core to the carbon shell are high. This leads to a greater amount of the electrons ejected from the silica core compared to carbon shell intensifying the silica peak compared to the carbon one. Moreover, the SiO_2 peak overlapping with the C (0 0 2) reflection peak of the carbon shell is excluded upon the core removal leading to the peak sharpening.

The mean size of crystallite of the carbon shells was calculated according to the line width of the C (0 0 2) plane refraction peak ($2\theta = 24.2^{\circ}$) using Scherrer Eq. (1) [29].

$$L = \frac{K\lambda}{\beta\cos\theta} \tag{1}$$

where L is the mean size of the crystallite, K is the dimensionless factor ($K = 0.9$), λ is the wavelength ($\lambda = 1.54$ Å), β is the full width at half maximum of the diffraction peak and θ is the diffraction angle. Additionally, the interlayer spacing of graphene structure of the carbon shell was calculated by Bragg law according to Eq. (2) [29].

$$n\lambda = 2d_{spacing}\sin\theta \ (or) \ d_{spacing} = \frac{n\lambda}{2\sin\theta} \tag{2}$$

where, d is the interlayer spacing, n is the positive integer (1), λ and θ are the wavelength ($\lambda = 1.54$ Å) and the peak position, respectively. It should be noted that the calculation of the interlayer spacing and number of layer have be performed for the main characteristic peak which is about 24.2° for graphene structure of CHS sample [55]. The values calculated by the Scherrer method and Bragg law for CHS sample is summarized in Table 2.

Accordingly, the mean crystallite size and interlayer spacing of the carbon shell values are ~15 and ~3.7 Å respectively, indicating that the number of graphene layers is ~5. The overall structure of graphite

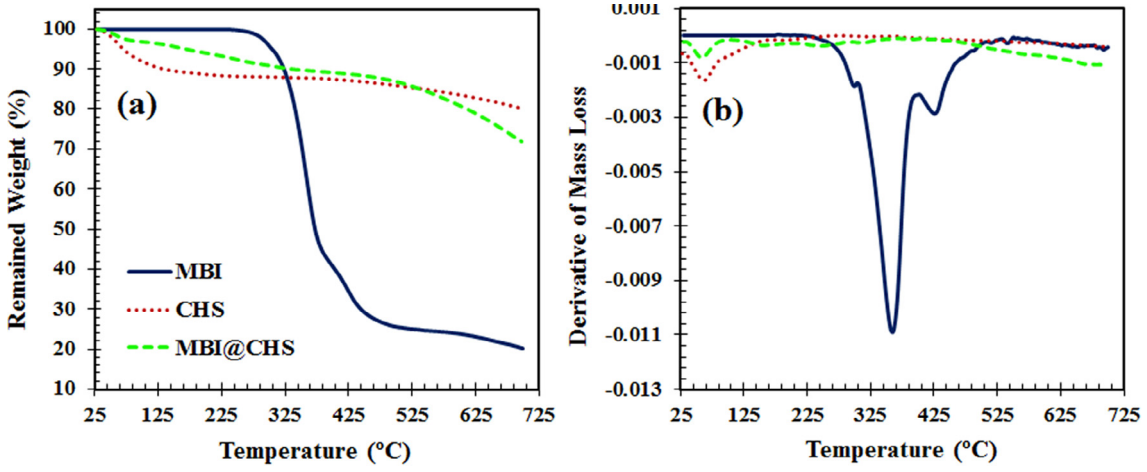

Fig. 8. TGA (a) and DTG (b) curves of MBI, CHS and MBI loaded carbon capsules.

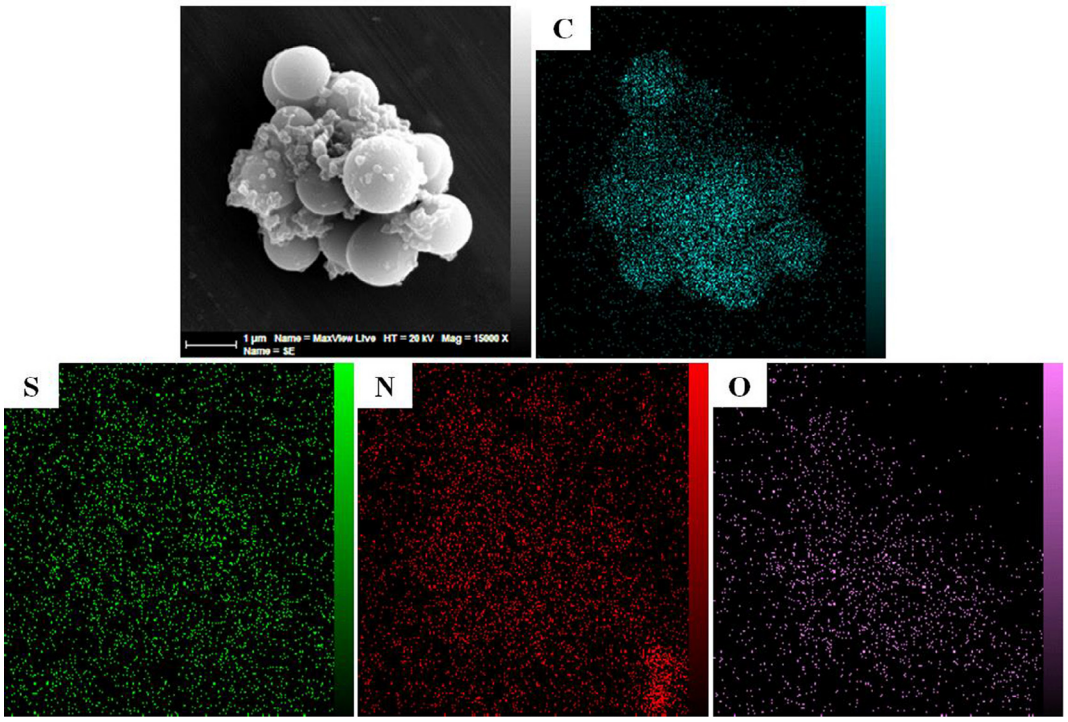

Fig. 9. FE-SEM image of MBI doped CHS and elemental mapping of C, S, N and O.

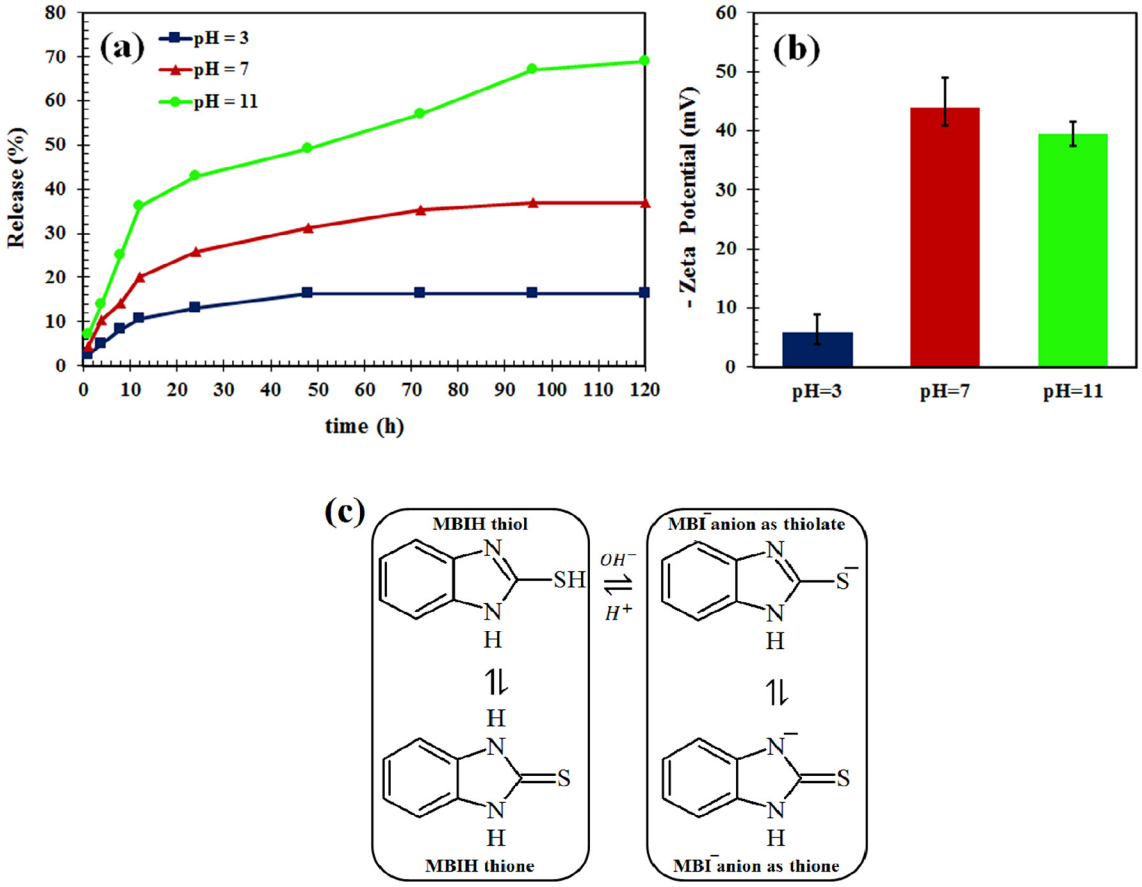

Fig. 10. Release kinetics of MBI from carbon capsules (10 mg) in the 3.5 wt% NaCl solution (10 ml) after 120 h at different pHs (a), zeta potential values of CHS at the different pHs (b) and the proposed deprotonation and protonation mechanism of MBI (c).

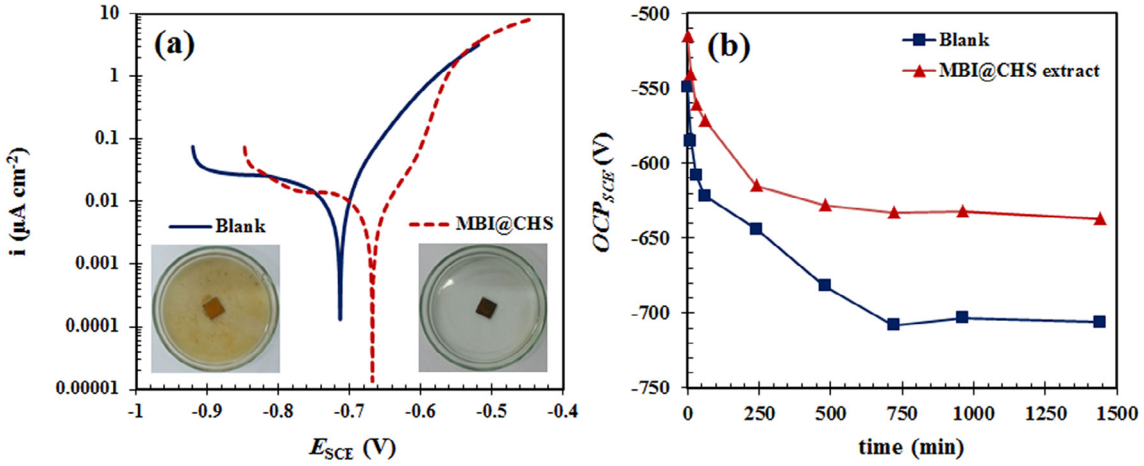

Fig. 11. Polarization curves of the mild steel samples after 24 h immersion (a) and OCP values (b) in the blank and MBI@CHS extract solutions.

Table 3
Electrochemical parameters obtained from the polarization curves of the mild steel samples versus the immersion time in blank and MBI@CHS extract solutions.

Sample	Time (h)	E_{corr} vs SCE (V)	i_{corr} (μA cm^{-2})	b_a (V/dec)	b_c (V/dec)	η (%)
Blank	1	−0.67	17.8	0.10	0.34	–
	4	−0.68	19.5	0.08	0.38	–
	24	−0.71	22.2	0.07	0.41	–
MBI@CHS	1	−0.64	11.5	0.07	0.42	35
	4	−0.63	9.6	0.07	0.35	51
	24	−0.64	8.0	0.07	0.34	64

and graphene is the same. Actually, graphite represents a stack of hundreds or even thousands layers of graphene. If the number of layers in stacks of graphite is limited e.g. less than 10, the characteristics of graphite is similar or close to that of graphene [56,57]. Therefore, the carbon structure of CHS synthesized in this work is more graphene-like. A scheme showing the graphene structure of CHS is provided in Fig. 6.

3.1.6. FTIR spectroscopy

FTIR spectroscopy was used to investigate the grafting of APTES onto the surface of the silica templates and CHSs. Surface modification of the silica templates was carried out to improve adsorption of the polysaccharide layer on the template surface. Also, surface modification of CHSs was performed to functionalize the surface of CHSs with amino groups. FTIR spectra of the silica templates and CHSs before and after surface modification are presented in Fig. 7. The wide peak at ~3471 cm^{-1} observed in the spectra of the modified silica templates and unmodified and modified CHS is attributed to vibration of the O—H stretching [58]. The peaks at ~2875 and ~2925 cm^{-1} are attributed to asymmetric stretching of C—H in the CHSs structure and CH_2 group of APTES [58,59]. The bands at ~790 and ~1640 cm^{-1} are attributed to N—H and $-NH_2$ groups originating from the amino groups of APTES [60]. The asymmetric vibrations of Si-O-Si network of the silica templates and the surface modified CHSs are detected at ~1075 cm^{-1} [58,61]. These indicate successful grafting of APTES.

3.2. Characterization of the MBI loaded CHSs

3.2.1. TGA

TGA analysis was conducted to quantify the amount of MBI doped into the CHSs. Fig. 8 shows the TGA and derivative TG (DTG) curves of MBI, empty carbon capsules and MBI doped CHSs. TGA and DTG curves of MBI show a two-step weight loss. The first prominent weight loss of MBI occurred at the temperature range of 270–380 °C due to the thermal decomposition of MBI and release of the degraded components which is about 68%. At temperatures higher than 425 °C, the remained components including aromatic carbon structures turn to ash with the value of ~21%. The TGA and DTG curves of CHSs illustrate a slight and steady weight loss between 25 and 125 °C and 125–425 °C attributed to the water removal from the surface and diffusing to the cavities and pores of CHSs (~9%) and thermal degradation of APTES grafted to the surface of CHSs (~2%). At temperatures above 550 °C, graphene sheets of the shells are subjected to thermal fracture leading to a partial release of volatile aromatic components, while the remaining weight of CHSs at 700 °C is ~81%.

It can be seen that the remaining weight for MBI@CHS between 25 and 525 °C is higher than that of CHS indicating a successfully loading of MBI into the cavities and pores of CHSs. Additionally, the thermal degradation of MBI occurs at a lower rate shifted to higher temperatures as compared to the pure MBI due to the inhibition of CHS shells. Moreover, due to the thermal degradation of MBI at higher temperatures, the remaining weight of MBI@CHS is lower than that of CHS. The 8% difference between the residue ash of CHS and MBI@CHS is attributed to MBI doped into CHSs. To confirm the encapsulation of MBI in CHSs, the solvent extraction method was used to determine the core content of MBI@CHSs using the process described below:

Firstly, a certain amount of MBI@CHS ($W_{MBI@CHS}$) was dispersed in acetone by a bath sonicator at ambient temperature. After 6 h of extraction, the extracted CHSs were carefully separated using the centrifugation and after complete draining the solvent and three times washing with ethanol, the extracted CHSs were dried in oven at 50 °C for 48 h. The final weight of the extracted CHSs (W_{CHS}) was recorded and the core content of MBI@CHSs was measured by Eq. (3).

$$Core\ content\ of\ MBI@CHSs = \frac{W_{MBI@CHS} - W_{CHS}}{W_{MBI@CHS}} \quad (3)$$

Based on calculation of the core content of MBI@CHS using Eq. (3), the MBI doped content in CHSs was estimated to be ~7.2 wt% which is in good agreement with the result obtained from the TGA analysis.

3.2.2. FE-SEM

Fig. 9 shows the FE-SEM images and the elemental mapping of MBI@CHS. The C elemental mapping is correlated to CHS shells. The C map depicts that the entire spherical form of CHSs remained the same after doping of MBI into the galleries of CHSs indicating sufficient mechanical strength of the carbon shell during the synthesizing procedure. Additionally, sulfur, nitrogen and oxygen are attributed to MBI doped in CHSs. The elemental maps demonstrated successful doping of MBI in the CHS shells.

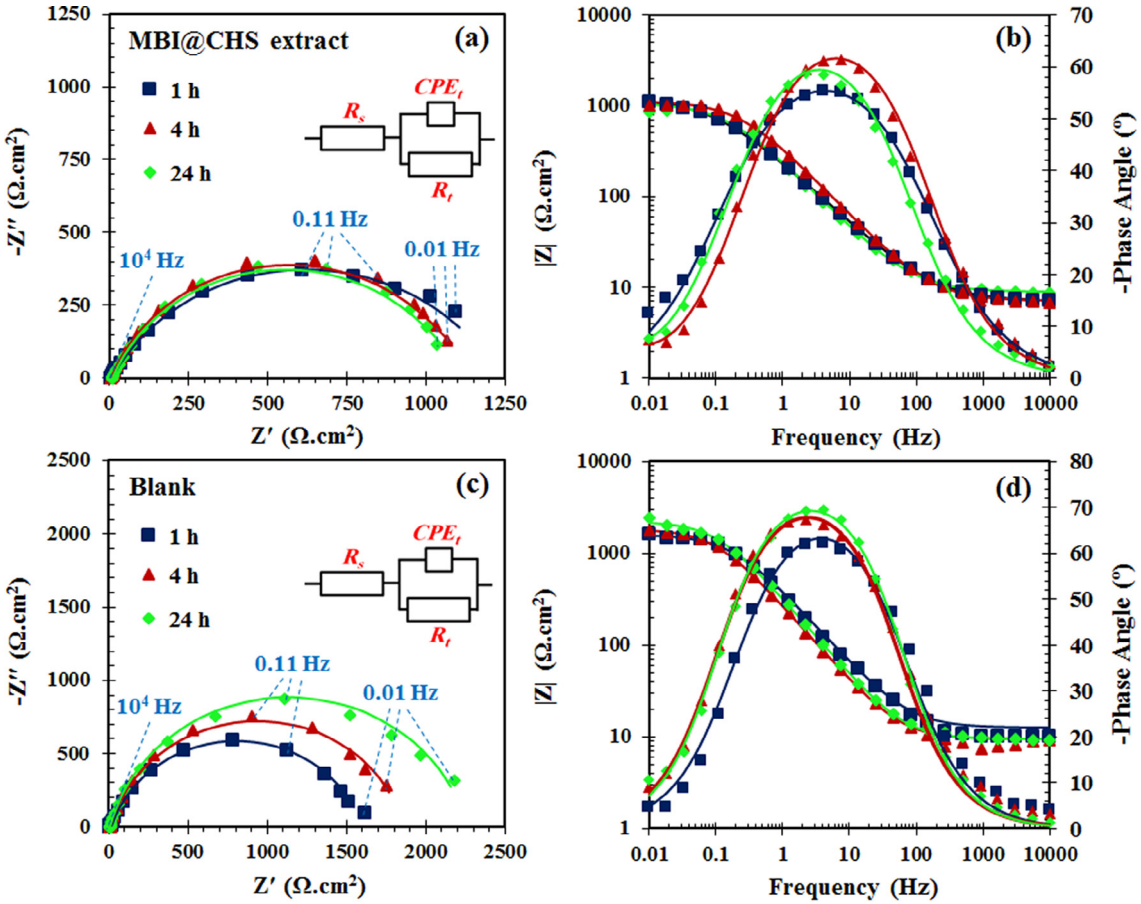

Fig. 12. Nyquist ((a) and (c)) and Bode ((b) and (d)) plots of mild steel samples immersed in the blank and MBI@CHS solutions for different immersion times. The markers and solid lines are the experimental and fitted data, respectively.

3.2.3. Release of MBI from the doped carbon capsules at different pHs

Release of MBI from the carbon capsules was investigated at different pHs. Fig. 10 shows the extent of MBI released within 120 h using UV–vis, zeta potential values of the carbon shells at different pHs and schematic deprotonation and protonation mechanisms of MBI. Fig. 10a shows release of MBI from the carbon capsules triggered at pH ~11. The release of MBI in the acidic solution (pH ~3) indicates suppression of MBI release from the inner cavities of the carbon capsules saving the doped MBI in the capsules, while the maximum release is obtained at the basic pH (pH ~11). Therefore, the MBI release from the capsules increases with the pH value indicating potential efficiency of the fabricated system for corrosion inhibition owing to the fact that corrosion of the metallic substrates in the neutral aqueous solutions comes with an increase of local pH due to the following cathodic reaction (Eq. (4)) [4]:

$$O_2 + 2H_2O + 4e^- \rightarrow 4OH^- \quad (4)$$

Fig. 10b shows that the zeta potential values of CHSs are negative at all pHs, while the zeta potential values increase with the order of pH ~7, pH ~11 and pH ~3. It is logical to assume that deprotonation of surface carboxylic acid groups of CHSs increases with increasing pH [62]. However, carboxylic acid groups are not the only chemical groups on the surface of CHSs. In fact, after removing the silica cores via acid treatment, the surface modification of CHSs with APTES was performed and a polysiloxane network was formed during the surface modification. The slight dissolution of the formed polysiloxane network at the alkaline solutions (pH = 11) is responsible for the slight change in the surface charge of CHSs. Consequently, the surface charge of CHSs at pH ~7 is more negative than pH ~11 due to the changing surface chemistry of CHSs. Deprotonation of the MBI molecules occurs at pH > 11 [63–65]. In fact, deprotonation of both thiol and thione groups of MBI molecules in the carbon capsules is responsible for the MBI release at pH ~11. This is due to the fact that negative charge of the carbon shell repels the negative charge of deprotonated MBI. Consequently, in alkaline solutions, deprotonation of MBI molecules results in the remarkable release of MBI in forms of thione and thiolate anions [64,66] as schematically shown in Fig. 10c.

3.3. Corrosion inhibition performance of MBI loaded carbon capsules

3.3.1. Potentiodynamic polarization and OCP measurements

The inhibition performance of MBI in the extract saline solution (3.5 wt% NaCl solution) was evaluated using potentiodynamic polarization and OCP measurements. Fig. 11 displays the polarization curves, corresponding images and OCP values of the mild steel samples after 24 h immersion in the blank and MBI@CHS extract solutions. The polarization curves indicate that both the anodic and cathodic activities are diminished in the presence of MBI@CHS extract, whereas the decrease of the anodic reaction is more pronounced than the cathodic one indicating a prevailing anodic inhibition of MBI@CHS. This phenomenon is in line with the observed shift of the corrosion potential to more positive values for the mild steel samples immersed in the MBI@CHS extract solution due to the adsorption of inhibitor on the surface. The electrochemical parameters including corrosion potential (E_{corr}), corrosion current density (i_{corr}), anodic Tafel slope (b_a) and cathodic Tafel slope (b_c) were derived from the polarization curves using Tafel extrapolation method and the results are summarized in Table 3. Inhibition efficiency (η) in this table was calculated according to Eq. (5) [9].

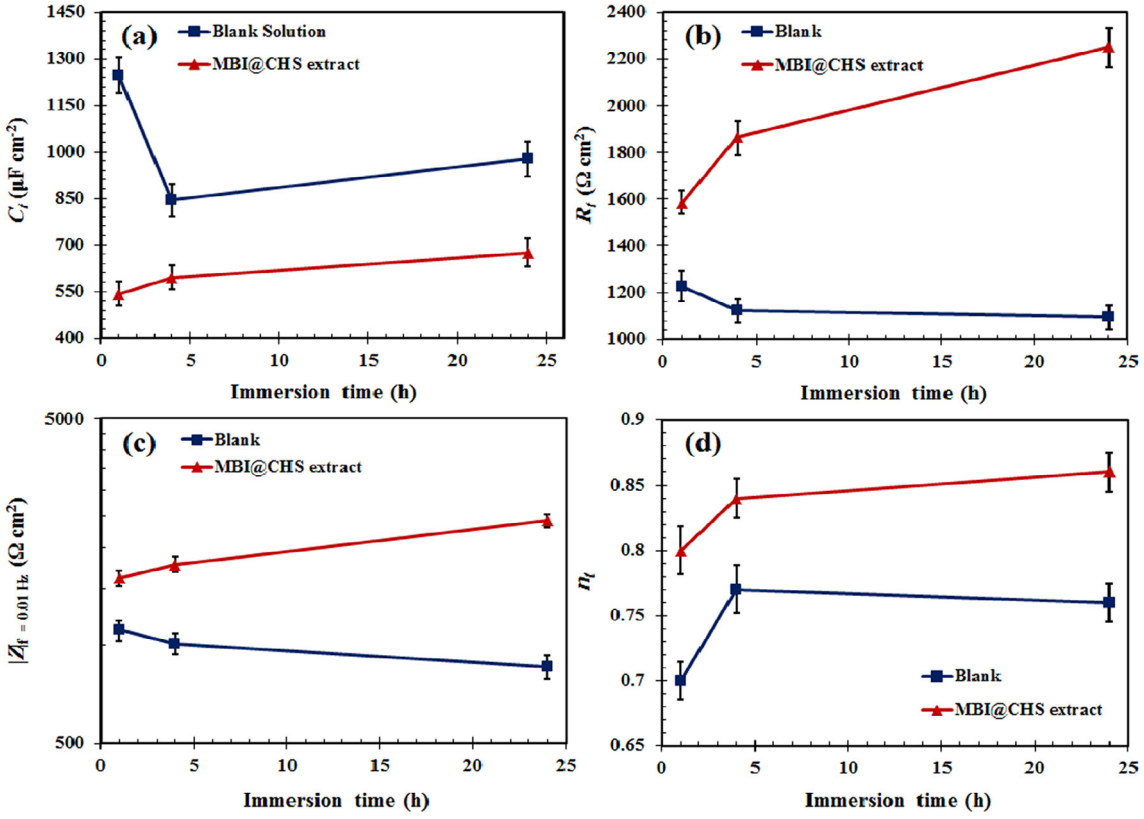

Fig. 13. C_t (a), R_t (b), $|Z|_{f=0.01\ Hz}$ (c) and n_t (d) values calculated from the EIS data of the mild steel samples immersed in the test solutions for different immersion times.

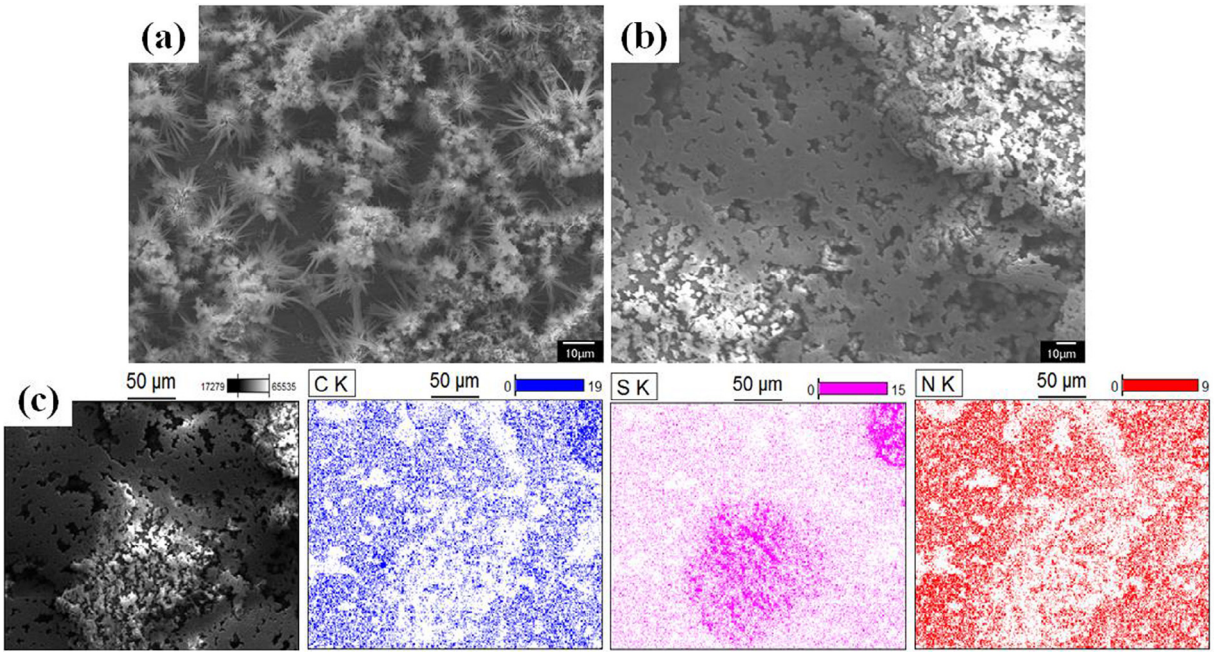

Fig. 14. FE-SEM micrograms of the mild steel samples after 24 h immersion in the 3.5 wt% NaCl solutions without (a) and with (b) MBI@CHS extract and the elemental mapping of C, S and N of the inhibited sample (c).

$$\eta(\%) = \left(1 - \left(\frac{i_{corr,i}}{i_{corr,b}}\right)\right) \times 100\% \quad (5)$$

In Eq. (5), $i_{corr,i}$ and $i_{corr,b}$ values are corrosion current densities of the samples in the corrosive solution with and without the MBI@CHS extract, respectively. The samples immersed in the MBI@CHS extract solution showed a decrease of the i_{corr} and an increase of η with immersion time indicating increasing inhibitor adsorption with exposure time. Fig. 11a shows that the mild steel sample dipped in the blank solution is covered with a corrosion product layer. Unlike the blank solution, the sample immersed in the extract solution exhibited no corrosion product due to inhibition by the MBI@CHS extract.

Table 4
Elemental weight percentage of the formed films on the samples immersed in the blank and inhibited solutions for 24 h.

Sample	O	C	N	S	Fe
Blank	25.5	–	–	–	balance
MBI@CHS extract	21.7	4.2	2.6	1.7	balance

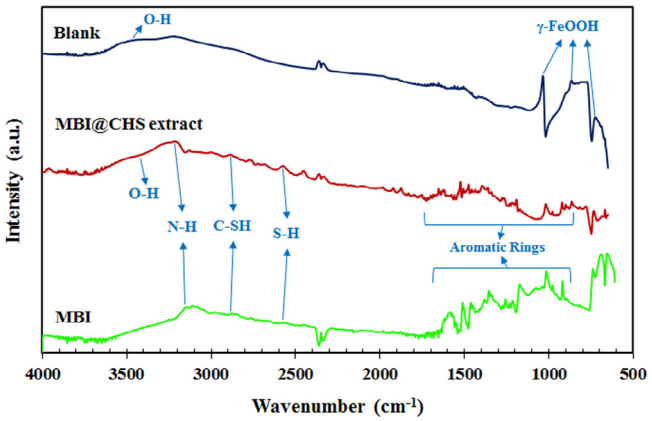

Fig. 15. FTIR spectra of the mild steel samples after 24 h immersion in the blank and MBI@CHS extract solutions and pure MBI.

Fig. 11b shows that the OCP values of the mild steel samples immersed in the MBI@CHS extract solution are more positive than of those immersed in the blank solution indicating an anodic protection of the MBI@CHS extract. This result indicates that the adsorption of MBI@CHS extract on the surface of the mild steel sample is responsible for the more positive values of OCP. For all samples immersed in the test solutions, a remarkable potential drop during the initial immersion times was observed which can be assigned to the initial metal surface oxidation and formation of electrical double layer. For the sample immersed in the corrosive solution with the MBI@CHS extract, the OCP values stabilized after 250 min immersion at around $-630\,mV_{SCE}$, while for the blank sample a steady trend was obtained after 750 min at a lower OCP value of around $-710\,mV_{SCE}$ indicating inhibition of the MBI@CHS extract in the saline solution.

3.3.2. EIS measurement

EIS measurement was employed to evaluate the corrosion inhibition of MBI@CHS in 3.5 wt% NaCl solution. Bare mild steel samples (1 cm^2) were immersed in the blank and MBI@CHS extract solutions for 1, 4 and 24 h. Fig. 12 shows the Nyquist and Bode plots of the EIS measurements. The increasing trend of the Nyquist semicircle diameters by time indicated a gradual formation of a MBI layer on the sample exposed to the MBI@CHS extract. The Nyquist plots indicated that the mild steel samples immersed in the extract solutions exhibited larger semicircles during all immersion times as compared to those of the blank solution revealing corrosion inhibition of the samples by MBI. All solutions exhibit one relaxation time during all immersion times. A one-time constant electrical equivalent circuit containing R_s (solution resistance), R_t (polarization resistance) and CPE_t (constant phase element) was used to fit the EIS data [9]. The double layer capacitance is calculated according to Eq. (6) [67].

$$C_t = \frac{(Q_0 \times R_t)^{1/n_t}}{R_t} \tag{6}$$

where C_t, Q_0, R_t and n_t are double layer capacitance, CPE admittance magnitude, total resistance (R_t = charge transfer resistance (R_{ct}) + inhibitor layer resistance (R_f)) and empirical exponent coefficient, respectively. The calculated C_t, R_t and low frequency impedance ($|Z|_{f\,=\,0.01\ Hz}$) values of the mild steel samples immersed in the test solutions for different immersion times are presented in Fig. 13. It can be seen that the lowest C_t and the highest R_t and $|Z|_{f\,=\,0.01\ Hz}$ values are obtained for the mild steel samples immersed in the MBI@CHS solution at all immersion times attributed to the adsorption of the released MBI from MBI@CHS on the mild steel surfaces. The significant decrease of C_t with immersion time for the samples immersed in MBI@CHS extract solution can be attributed to the formation of a protective inhibitor-containing layer on the metal surface. As shown in Fig. 13c, immersion in the extract solution resulted in increase of $|Z|_{f\,=\,0.01\ Hz}$ values due to increase of the surface coverage by the inhibitor. According to Fig. 13d, the n_t values of the samples immersed in the extract solution are higher than those of the blank solution due to the lower surface heterogeneity [68,69]. These observations are in good agreement with the potentiodynamic polarization and OCP measurements.

3.3.3. FE-SEM

Fig. 14 shows the morphology of mild steel surfaces after 24 h immersion in the blank and MBI@CHS extract solutions. The elemental composition of the corrosion products extracted from the EDS analyses

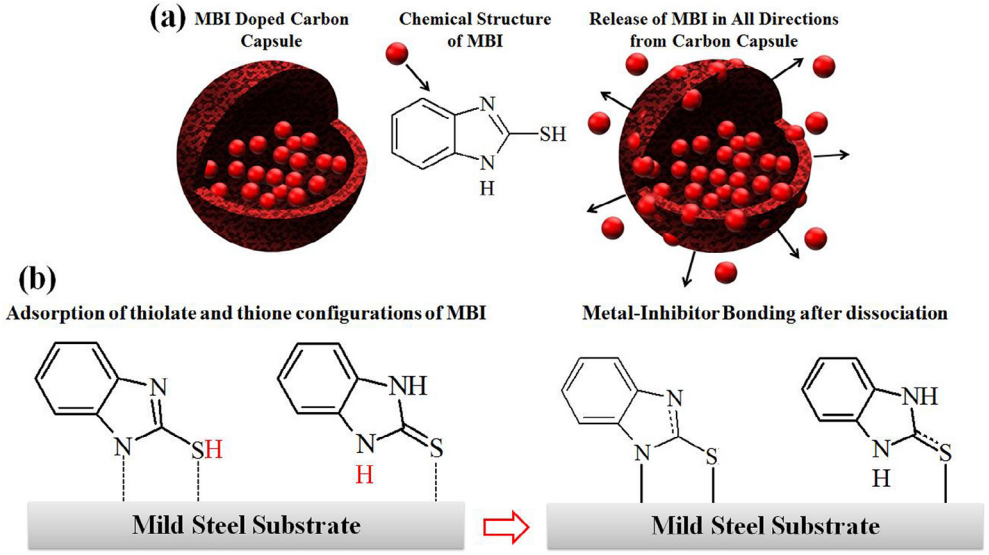

Fig. 16. Schematic illustration of MBI release from CHSs (a) and the consequent adsorption of thiolate and thione configurations of MBI on the mild steel surface (b).

are summarized in Table 4. It can be seen that sediments were formed on the samples immersed in both blank and extract solutions. The different morphologies of the sediments on the blank and inhibited samples indicated formation of a protective layer on the inhibited sample with lower roughness and porosity. EDS-mapping analyses showed the presence of C, S and N on the inhibited sample verifying the release and consequently deposition of MBI. Additionally, the lower concentration of O on the inhibited sample than the blank one implied a lower amount of oxidation or corrosion [9] which in-turn verifies the inhibitive action of MBI.

3.3.4. Confocal FTIR

FTIR spectra of the mild steel samples immersed in the blank and inhibited solutions for 24 h are shown in Fig. 15. Several additional peaks were observed in the FTIR spectrum of the sample exposed in the extract solution as compared to that of exposed in the blank solution indicating the presence of MBI on the inhibited sample. The broad absorption peak at 2800–3600 cm^{-1} of the sample exposed in the blank solution originated from the O—H groups while that of the inhibited spectrum overlapped with N—H stretching band at 3400 cm^{-1} originating from MBI [23]. The peaks of lepidocrocite (γ-FeOOH) observed at 765, 863 and 1026 cm^{-1} [23] of the blank sample can hardly be detected for the inhibited sample indicating different surface chemistry due to the adsorption of MBI. The peaks at 2579 and 1845 cm^{-1} can also be assigned to the S-H and C-SH stretching of MBI [23,60]. Moreover, the shoulders observed at 800–1000 cm^{-1} and 1200–1600 cm^{-1} were correlated to the carbon-carbon bonds of the MBI aromatic structure adsorbed on the surface [60].

Fig. 16 schematically shows the CHSs doped with MBI as well as the possible adsorption of the released MBI in forms of thiolate and thione on the mild steel surface. The permeable structure of the CHSs allowed a gradual release of MBI through the porous structure of CHSs providing corrosion inhibition. The inhibitor release occurred in a wide range of pHs, especially at high local pH values, reacting with the metal surface and consequently retarding corrosion.

4. Conclusions

In the present work, a new generation of graphene-structured capsules based on carbon hollow spheres (CHSs) was synthesized via silica templating method for corrosion protection applications. Synthesis of CHSs was performed using polymerization of sucrose and carbonization of polysaccharide shells onto the silanized silica templates. Raman spectroscopy and XRD results revealed formation of graphene-structured shells with low structural defects. It was shown that the surface modification of silica templates contributes to the formation of shells with sp^2 carbon structures providing favorable mechanical properties for subsequent MBI doping. The pH responsive release of MBI from CHSs was observed at pH ~11 indicating a high potential of MBI-doped CHSs for corrosion inhibition of mild steel which was verified by the electrochemical measurements. Moreover, FE-SEM/EDS and local FTIR results proved adsorption of the released MBI onto the surface of the mild steel samples after 24 h immersion in the MBI-doped CHSs extract solution.

References

[1] B.J. Blaiszik, S.L.B. Kramer, S.C. Olugebefola, J.S. Moore, N.R. Sottos, S.R. White, Self-healing polymers and composites, Annu. Rev. Mater. Res. 40 (2010) 179–211.

[2] D. Grigoriev, D. Akcakayiran, M. Schenderlein, D. Shchukin, Protective organic coatings with anticorrosive and other feedback-active features: micro-and nano-containers-based approach, Corrosion 70 (2013) 446–463.

[3] S.A. Haddadi, M. Mahdavian, E. Karimi, Evaluation of the corrosion protection properties of an epoxy coating containing sol–gel surface modified nano-zirconia on mild steel, RSC Adv. 5 (2015) 28769–28777.

[4] N. Pirhady Tavandashti, M. Ghorbani, A. Shojaei, J.M.C. Mol, H. Terryn, K. Baert, Y. Gonzalez-Garcia, Inhibitor-loaded conducting polymer capsules for active corrosion protection of coating defects, Corros. Sci. 112 (2016) 138–149.

[5] Y. Feng, Y.F. Cheng, An intelligent coating doped with inhibitor-encapsulated nanocontainers for corrosion protection of pipeline steel, Chem. Eng. J. 315 (2017) 537–551.

[6] K. Kermannezhad, A.N. Chermahini, M.M. Momeni, B. Rezaei, Application of amine-functionalized MCM-41 as pH-sensitive nano container for controlled release of 2-mercaptobenzoxazole corrosion inhibitor, Chem. Eng. J. 306 (2016) 849–857.

[7] M.A. Migahed, M.M. El-Rabiei, H. Nady, M. Fathy, Synthesis, characterization of some ethoxylated tolyltriazole derivatives and evaluation of their performance as corrosion inhibitors for Cu-10Al alloy in seawater, J. Environ. Chem. Eng. 4 (2016) 3741–3752.

[8] E. Alibakhshi, E. Ghasemi, M. Mahdavian, The influence of surface modification of lithium zinc phosphate pigment on corrosion inhibition of mild steel and adhesion strength of epoxy coating, J. Sol-Gel Sci. Technol. 72 (2014) 359–368.

[9] E. Alibakhshi, E. Ghasemi, M. Mahdavian, B. Ramezanzadeh, S. Farashi, Active corrosion protection of Mg-Al-PO43−LDH nanoparticle in silane primer coated with epoxy on mild steel, J. Taiwan Inst. Chem. Eng. 75 (2017) 248–262.

[10] D.G. Shchukin, S.V. Lamaka, K.A. Yasakau, M.L. Zheludkevich, M.G.S. Ferreira, H. Möhwald, Active anticorrosion coatings with halloysite nanocontainers, J. Phys. Chem. C 112 (2008) 958–964.

[11] A. Ghazi, E. Ghasemi, M. Mahdavian, B. Ramezanzadeh, M. Rostami, The application of benzimidazole and zinc cations intercalated sodium montmorillonite as smart ion exchange inhibiting pigments in the epoxy ester coating, Corros. Sci. 94 (2015) 207–217.

[12] C. Zea, R. Barranco-García, B. Chico, I. Díaz, M. Morcillo, D. de la Fuente, Smart mesoporous silica nanocapsules as environmentally friendly anticorrosive pigments, Int. J. Corros. 2015 (2015).

[13] H. Yi, Y. Deng, C. Wang, Pickering emulsion-based fabrication of epoxy and amine microcapsules for dual core self-healing coating, Compos. Sci. Technol. 133 (2016) 51–59.

[14] M. Samadzadeh, S.H. Boura, M. Peikari, A. Ashrafi, M. Kasiriha, Tung oil: an autonomous repairing agent for self-healing epoxy coatings, Prog. Org. Coat. 70 (2011) 383–387.

[15] N. Pirhady Tavandashti, M. Ghorbani, A. Shojaei, Y. Gonzalez-Garcia, H. Terryn, J.M.C. Mol, PH responsive Ce(III) loaded polyaniline nanofibers for self-healing corrosion protection of AA2024-T3, Prog. Org. Coat. 99 (2016) 197–209.

[16] J. Tedim, S.K. Poznyak, A. Kuznetsova, D. Raps, T. Hack, M.L. Zheludkevich, M.G.S. Ferreira, Enhancement of active corrosion protection via combination of inhibitor-loaded nanocontainers, ACS Appl. Mater. Interfaces. 2 (2010) 1528–1535.

[17] S.E. Karekar, U.D. Bagale, S.H. Sonawane, B.A. Bhanvase, D.V. Pinjari, A smart coating established with encapsulation of Zinc Molybdate centred nanocontainer for active corrosion protection of mild steel: release kinetics of corrosion inhibitor, Compos. Interfaces (2018) 1–24.

[18] A.J. Jadhav, C.R. Holkar, D.V. Pinjari, Anticorrosive performance of super-hydrophobic imidazole encapsulated hollow zinc phosphate nanoparticles on mild steel, Prog. Org. Coat. 114 (2018) 33–39.

[19] A.J. Jadhav, S.E. Karekar, D.V. Pinjari, Y.G. Datar, B.A. Bhanvase, S.H. Sonawane, A.B. Pandit, Development of smart nanocontainers with a zinc phosphate core and a ph-responsive shell for controlled release of immidazole, Hybrid Mater. 2 (2015).

[20] A.J. Jadhav, D.V. Pinjari, A.B. Pandit, Surfactant assisted sonochemical synthesis of hollow structured zinc phosphate nanoparticles and their application as nano-carrier, Chem. Eng. J. 297 (2016) 116–120.

[21] A.C. Balaskas, I.A. Kartsonakis, D. Snihirova, M.F. Montemor, G. Kordas, Improving the corrosion protection properties of organically modified silicate–epoxy coatings by incorporation of organic and inorganic inhibitors, Prog. Org. Coat. 72 (2011) 653–662.

[22] E. Shchukina, D. Shchukin, D. Grigoriev, Effect of inhibitor-loaded halloysites and mesoporous silica nanocontainers on corrosion protection of powder coatings, Prog. Org. Coat. 102 (2017) 60–65.

[23] M. Mahdavian, S. Ashhari, Mercapto functional azole compounds as organic corrosion inhibitors in a polyester-melamine coating, Prog. Org. Coat. 68 (2010) 259–264.

[24] S. Ravi, S. Vadukumpully, Sustainable carbon nanomaterials: recent advances and its applications in energy and environmental remediation, J. Environ. Chem. Eng. 4 (2016) 835–856.

[25] H.O. Pierson, Handbook of Carbon, Graphite, Diamond and by, (n.d.).

[26] S. Li, A. Pasc, V. Fierro, A. Celzard, Hollow carbon spheres, synthesis and applications- a review, J. Mater. Chem. A 4 (2016) 12686–12713.

[27] C. Zhang, L. Wang, Y. Zhao, Y. Tian, J. Liang, Self-assembly synthesis of graphene oxide double-shell hollow-spheres decorated with Mn3O4 for electrochemical supercapacitors, Carbon N. Y. 107 (2016) 100–108.

[28] A.F. Arif, Y. Kobayashi, R. Balgis, T. Ogi, H. Iwasaki, K. Okuyama, Rapid microwave-assisted synthesis of nitrogen-functionalized hollow carbon spheres with high monodispersity, Carbon N. Y. 107 (2016) 11–19.

[29] R. Atchudan, S. Perumal, T.N. Jebakumar Immanuel Edison, Y.R. Lee, Facile synthesis of monodisperse hollow carbon nanospheres using sucrose by carbonization route, Mater. Lett. 166 (2016) 145–149.

[30] P. Li, J. Liu, Y. Wang, Y. Liu, X. Wang, K.W. Nam, Y.M. Kang, M. Wu, J. Qiu, Synthesis of ultrathin hollow carbon shell from petroleum asphalt for high-performance anode material in lithium-ion batteries, Chem. Eng. J. 286 (2016) 632–639.

[31] M. Liu, M. Shi, W. Lu, D. Zhu, L. Li, L. Gan, Core–shell reduced graphene oxide/MnOx@ carbon hollow nanospheres for high performance supercapacitor electrodes, Chem. Eng. J. 313 (2017) 518–526.

[32] J. Yao, T. Mei, Z. Cui, Z. Yu, K. Xu, X. Wang, Hollow carbon spheres with TiO2 encapsulated sulfur and polysulfides for long-cycle lithium-sulfur batteries, Chem. Eng. J. 330 (2017) 644–650.

[33] W. Yang, H. Zhao, L. Chen, C. Fang, Z. Rui, L. Yang, H. Wan, J. Liu, Y. Zhou,

P. Wang, Ferrous sulfide-assisted hollow carbon spheres as sulfur host for advanced lithium-sulfur batteries, Chem. Eng. J. 326 (2017) 1040–1047.
[34] X.W. Lou, D. Deng, J.Y. Lee, L.A. Archer, Preparation of SnO2/carbon composite hollow spheres and their lithium storage properties, Chem. Mater. (2008) 6562–6566.
[35] T. Jaumann, M. Herklotz, M. Klose, K. Pinkert, S. Oswald, J. Eckert, L. Giebeler, Tailoring hollow silicon-carbon nanocomposites as high-performance anodes in secondary lithium-based batteries through economical chemistry, Chem. Mater. 27 (2015) 37–43.
[36] J. Lv, X. Yang, H. Zhou, L. Kang, Z. Lei, Z.H. Liu, MnO2-wrapped hollow graphitized carbon nanosphere electrode for supercapacitor, Mater. Res. Bull. 73 (2016) 429–436.
[37] M. Klose, R. Reinhold, K. Pinkert, M. Uhlemann, F. Wolke, J. Balach, T. Jaumann, U. Stoeck, J. Eckert, L. Giebeler, Hierarchically nanostructured hollow carbon nanospheres for ultra-fast and long-life energy storage, Carbon N. Y. 106 (2016) 306–313.
[38] Y.K. Huang, C.H. Su, J.J. Chen, C.T. Chang, Y.H. Tsai, S.F. Syu, T.T. Tseng, C.S. Yeh, Fabrication of silica-coated hollow carbon nanospheres encapsulating Fe3O4 cluster for magnetical and MR imaging guided NIR light triggering hyperthermia and ultrasound imaging, ACS Appl. Mater. Interfaces. 8 (2016) 14470–14480.
[39] N.A. Katcho, E. Urones-Garrote, D. Avila-Brande, A. Gomez-Herrero, S. Urbonaite, S. Csillag, E. Lomba, F. Agullo-Rueda, A.R. Landa-Canovas, L.C. Otero-Diaz, Carbon hollow nanospheres from chlorination of ferrocene, Chem. Mater. 19 (2007) 2304–2309.
[40] D. Yuan, C. Xu, Y. Liu, S. Tan, X. Wang, Z. Wei, P.K. Shen, Synthesis of coin-like hollow carbon and performance as Pd catalyst support for methanol electrooxidation, Electrochem. Commun. 9 (2007) 2473–2478.
[41] S. Ikeda, K. Tachi, Y.H. Ng, Y. Ikoma, T. Sakata, H. Mori, T. Harada, M. Matsumura, Selective adsorption of glucose-derived carbon precursor on amino-functionalized porous silica for fabrication of hollow carbon spheres with porous walls, Chem. Mater. 19 (2007) 4335–4340.
[42] A. Chen, Y. Li, Y. Yu, Y. Li, K. Xia, Y. Wang, S. Li, L. Zhang, Synthesis of hollow mesoporous carbon spheres via “dissolution-capture” method for effective phenol adsorption, Carbon N. Y. 103 (2016) 157–162.
[43] G. Cheng, M. Da Zhou, S.Y. Zheng, Facile synthesis of magnetic mesoporous hollow carbon microspheres for rapid capture of low-concentration peptides, ACS Appl. Mater. Interfaces. 6 (2014) 12719–12728.
[44] W. Stöber, A. Fink, E. Bohn, Controlled growth of monodisperse silica spheres in the micron size range, J. Colloid Interface Sci. 26 (1968) 62–69.
[45] X. Sun, Y. Li, Colloidal carbon spheres and their core/shell structures with noble-metal nanoparticles, Angew. Chemie Int. Ed. 43 (2004) 597–601.
[46] J.R. Matos, M. Kruk, L.P. Mercuri, M. Jaroniec, L. Zhao, T. Kamiyama, O. Terasaki, T.J. Pinnavaia, Y. Liu, Ordered mesoporous silica with large cage-like pores: structural identification and pore connectivity design by controlling the synthesis temperature and time, J. Am. Chem. Soc. 125 (2003) 821–829.
[47] X. Li, F. Luo, G. He, Activation of the solid silica layer of aerosol-based C/SiO2 particles for preparation of various functional multishelled hollow microspheres, Langmuir 31 (2015) 5164–5173.
[48] B. Fang, M. Kim, J.H. Kim, J. Yu, Controllable Synthesis of Hierarchical Nanostructured Hollow Core/Mesopore Shell Carbon for Electrochemical Hydrogen Storage Controllable Synthesis of Hierarchical Nanostructured Hollow Core/Mesopore Shell Carbon for Electrochemical Hydrogen Storage, Synthesis (Stuttg). (2008) 12068–12072.
[49] A.C. Ferrari, D.M. Basko, Raman spectroscopy as a versatile tool for studying the properties of graphene, Nat. Nanotechnol. 8 (2013) 235–246.
[50] K.N. Kudin, B. Ozbas, H.C. Schniepp, R.K. Prud’homme, I.A. Aksay, R. Car, Raman spectra of graphite oxide and functionalized graphene sheets, Nano Lett. 8 (2008) 36–41.
[51] A.C. Ferrari, Raman spectroscopy of graphene and graphite: disorder, electron-phonon coupling, doping and nonadiabatic effects, Solid State Commun. 143 (2007) 47–57.
[52] Z. Ni, Y. Wang, T. Yu, Z. Shen, Raman spectroscopy and imaging of graphene, Nano Res. 1 (2008) 273–291.
[53] U. Zulfiqar, T. Subhani, S.W. Husain, Synthesis and characterization of silica nanoparticles from clay, J. Asian Ceram. Soc. 4 (2016) 91–96.
[54] R. Atchudan, A. Pandurangan, Growth of ordered multi-walled carbon nanotubes over mesoporous 3D cubic Zn/Fe-KIT-6 molecular sieves and its use in the fabrication of epoxy nanocomposites, Microporous Mesoporous Mater. 167 (2013) 162–175.
[55] F.T. Johra, J.-W. Lee, W.-G. Jung, Facile and safe graphene preparation on solution based platform, J. Ind. Eng. Chem. 20 (2014) 2883–2887.
[56] M.J. Allen, V.C. Tung, R.B. Kaner, Review of Graphene, Chem. Rev. 110 (2010) 132–145.
[57] M.J. Allen, V.C. Tung, R.B. Kaner, Honeycomb carbon: a review of graphene, Chem. Rev. 110 (2009) 132–145.
[58] S.A. Haddadi, S.A.A. Ramazani, M. Amini, A. Kheradmand, In-situ preparation and characterization of ultra-high molecular weight polyethylene/diamond nanocomposites using Bi-supported Ziegler-Natta catalyst: effect of nanodiamond silanization, Mater. Today Commun. 14 (2017) 53–64.
[59] S.A. Haddadi, M. Mahdavian-ahadi, F. Abbasi, Effect of nanosilica and boron carbide on adhesion strength of high temperature adhesive based on phenolic resin for graphite bonding, Ind. Eng. Chem. Res. 53 (2014) 11747–11754.
[60] D.L. Pavia, Introduction to spectroscopy, CengageBrain. com. (2009).
[61] S.A. Haddadi, S.A.A Ramazani, S. Talebi, S. Fattahpour, M. Hasany, Investigation of the effect of nanosilica on rheological, thermal, mechanical, structural, and piezoelectric properties of PVDF nanofibers fabricated using electrospinning technique, Ind. Eng. Chem. Res. 56 (2017) 12596–12607.
[62] B. Konkena, S. Vasudevan, Understanding aqueous dispersibility of graphene oxide and reduced graphene oxide through p K a measurements, J. Phys. Chem. Lett. 3 (2012) 867–872.
[63] R.K. Shervedani, A. Hatefi-Mehrjardi, M.K. Babadi, Comparative electrochemical study of self-assembled monolayers of 2-mercaptobenzoxazole, 2-mercaptobenzothiazole, and 2-mercaptobenzimidazole formed on polycrystalline gold electrode, Electrochim. Acta. 52 (2007) 7051–7060.
[64] M. Finšgar, 2-Mercaptobenzimidazole as a copper corrosion inhibitor: Part II. Surface analysis using X-ray photoelectron spectroscopy, Corros. Sci. 72 (2013) 90–98.
[65] M. Mahdavian, R. Naderi, M. Peighambari, M. Hamdipour, S.A. Haddadi, Evaluation of cathodic disbondment of epoxy coating containing azole compounds, J. Ind. Eng. Chem. 21 (2015) 1167–1173.
[66] P.M. Niamien, H.A. Kouassi, A. Trokourey, F.K. Essy, D. Sissouma, Y. Bokra, Copper Corrosion Inhibition in 1 M HNO3 by Two Benzimidazole Derivatives, ISRN Mater. Sci. 2012 (2012).
[67] B. Hirschorn, M.E. Orazem, B. Tribollet, V. Vivier, I. Frateur, M. Musiani, Determination of effective capacitance and film thickness from constant-phase-element parameters, Electrochim. Acta. 55 (2010) 6218–6227.
[68] I.B. Obot, N.O. Obi-Egbedi, A.O. Eseola, Anticorrosion potential of 2-mesityl-1H-imidazo [4, 5-f][1, 10] phenanthroline on mild steel in sulfuric acid solution: experimental and theoretical study, Ind. Eng. Chem. Res. 50 (2011) 2098–2110.
[69] J.R. Macdonald, Impedance spectroscopy and its use in analyzing the steady-state AC response of solid and liquid electrolytes, J. Electroanal. Chem. Interfacial Electrochem. 223 (1987) 25–50.